Journal of Alloys and Compounds 931 (2023) 167542

Contents lists available at ScienceDirect

Journal of Alloys and Compounds

journal homepage: www.elsevier.com/locate/jalcom

Fabrication of spherical MoNbTaWZr refractory high-entropy powders by spray granulation combined with plasma spheroidization

Ming Xia [a,b,d], Yongxiong Chen [b], Rong Wang [b], Xiubing Liang [b,*], Baolong Shen [c,d,**]

[a] School of Chemical Engineering and Technology, China University of Mining and Technology, Xuzhou 221116, PR China
[b] Defense Innovation Institute, Academy of Military Science, Beijing 100071, PR China
[c] School of Materials Science and Engineering, Jiangsu Key Laboratory for Advanced Metallic Materials, Southeast University, Nanjing 211189, PR China
[d] School of Materials Science and Physics, China University of Mining and Technology, Xuzhou 221116, PR China

ARTICLE INFO

Article history:
Received 30 August 2022
Accepted 9 October 2022
Available online 12 October 2022

Keywords:
Refractory high-entropy alloy
Spherical MoNbTaWZr powder
Spray granulation
Plasma spheroidization

ABSTRACT

To obtain spherical MoNbTaWZr powders, porous agglomerated MoNbTaWZr particles prepared by spray granulation were subsequently processed by plasma spheroidization. The microstructure, morphology, particle size distribution, purity and property of each step during process were systematically investigated. Results show that the obtained spherical MoNbTaWZr powder has dense structure, smooth surface, and good sphericity in shape. It also has narrow particle size distribution, while D_{10}, D_{50}, D_{90} and D_{av} were 32.0 μm, 42.3 μm, 56.0 μm and 43.2 μm, respectively. The powder has a high purity, and the concentration of oxygen, hydrogen, carbon, and nitrogen were all at ppm. In addition, excellent flowability (8.89 s/50 g) and apparent density (7.27 g/cm^3) are benefit from high spheroidization ratio (98.4 %) and dense structure. The spherical powder also exhibits a high nano-hardness due to solid solution strengthening and refinement in dendritic structures.

1. Introduction

With the continuous increasing demands in high performance materials using in harsh environments, a fantastic material, called high-entropy alloys (HEAs) was proposed by Yeh et al. and Cantor et al. in 2004 [1,2]. Different with traditional alloys, HEAs are composed of five or more primary elements with equimolar or near-equimolar atomic ratios. Generally, multi principal elements might form intermetallic compounds, however, HEAs tend to form a simple solid solution as a result of high-mixing-entropy effect and the prediction of Gibbs free energy according to the mutual solubility of the constituent elements [3,4]. Additionally, HEAs have received tremendous attractions because of their outstanding properties, for instance, high strength and ductility, superior wear and corrosion resistance, and splendid radiation resistance [5–10]. Body-centered cubic (BCC) refractory high-entropy alloys (RHEAs) based on the composition of Mo, Nb, Ta, and W is one of the hottest systems because of the higher yield strength at elevated temperatures [11]. However, the poor room-temperature plasticity hinders their further development. This dilemma is believed to be coped with the back-stress induced by hetero-deformation effect. Heterogeneous structure (HS) containing soft and hard regions has proven to be an effective approach in improving the plasticity of BCC RHEAs [12,13]. To achieve this goal in MoNbTaW-based RHEAs, we investigated the mechanical properties of MoNbTaWX (X = Cr, Zr, V, Hf, and Re) by combination of first-principles calculations and experiments. As a result, Zr has a relatively low valence electron concentration (VEC), which helps to transform intrinsic brittleness into intrinsic ductility [14]. And larger atomic radius of Zr than Mo, Nb, Ta, and W makes it easy to generate elements segregation to form HS due to lattice distortions [15]. Therefore, MoNbTaWZr RHEA has shown good combination of compressive yield strength (1480 MPa) and peak strain (15.9 %) superior to other MoNbTaW-based RHEAs indeed [16].

Besides arc melting and sintering, other versatile methodologies to fabricate RHEAs are powder-based processes, such as, powder metallurgy (PM), additive manufacturing (AM), and thermal spraying, thus promoting the further development of metal powder. Various attempts have been applied to synthesis RHEA powders including a simple mix of elemental powders, mechanical alloying, and high energy ball milling [17–19]. The requirements of powders used for fabricating RHEAs should be with spherical shape, optimized size, and high purity due to the mechanical properties of

* Corresponding author.
** Corresponding author at: School of Materials Science and Engineering, Jiangsu Key Laboratory for Advanced Metallic Materials, Southeast University, Nanjing 211189, PR China.
E-mail addresses: liangxb_d@163.com (X. Liang), blshen@seu.edu.cn (B. Shen).

https://doi.org/10.1016/j.jallcom.2022.167542
0925-8388/

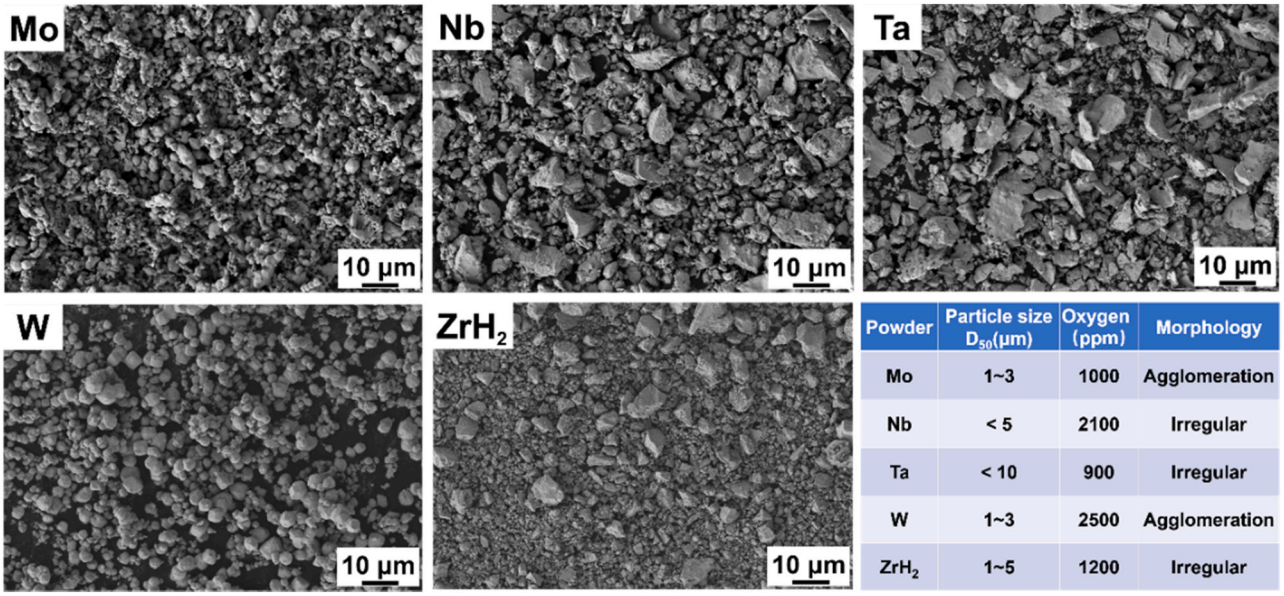

Powder	Particle size D_{50}(μm)	Oxygen (ppm)	Morphology
Mo	1~3	1000	Agglomeration
Nb	< 5	2100	Irregular
Ta	< 10	900	Irregular
W	1~3	2500	Agglomeration
ZrH_2	1~5	1200	Irregular

Fig. 1. SEM images of the five different raw powders and the corresponding physical characteristics.

RHEAs and the efficiency of the process depend on the quality of the powder [3,20]. However, alloy powders prepared by all above mentioned techniques have some inevitable disadvantages, such as large amounts of contaminants, long time milling. Therefore, it is of great essential to look for other practical method. Meanwhile, spherical MoNbTaW RHEA powder with a dense structure were successfully prepared using spray granulation combined with plasma spheroidization techniques, which was a feasible way to control the morphology, particle size distribution and purity [21]. As we all know, spray granulation and plasma spheroidization techniques enable high efficiency of mass-production, appropriate particle size distribution, and high-quality spherical powders with relative low cost [22]. Thus, spray granulation combining plasma spheroidization were employed to prepare spherical MoNbTaWZr RHEA powder.

In the present research, spherical MoNbTaWZr RHEA powder was firstly fabricated by spray granulation (SG) combined with plasma spheroidization (PS). The raw materials were firstly blend with polyvinyl alcohol (PVA) and sodium lignosulfonate (SL) by colloid grinder to obtain highly dispersed slurry. Then the highly dispersed slurry was spray granulated to achieve nearly spherical MoNbTaWZr RHEA powder. Finally, spheroidized MoNbTaWZr RHEA powder was prepared by plasma spheroidization. Microstructure, phase composition, morphology, particle size, and purity dependent formation mechanism were discussed. This work can be considered as a baseline for researchers to fabricate other spherical RHEA powders which has large discrepancy in element melting points using similar method.

2. Experimental

2.1. Powder preparation

Starting powders were commercial fine elemental Mo, Nb, Ta, W and hydride Zr powders. The morphology and physical characteristics of the raw powders are shown in Fig. 1. According to the SEM images, powders of Mo and W were found in the form of loosely agglomerated particles, while others were irregular. The purity of all powders was over 99.9 % and the particle size were less than 10 μm. A schematic diagram of spherical powder preparation procedure is illustrated in Fig. 2. At beginning of the experiment, the powders were mixed with colloidal solution which contains alcohol, certain ratio of SL, and PVA to form a slurry. The PVA concentration and the solid content were 3 wt % and 55 wt %, respectively. Content of the SL in the slurry was smaller than 2 %. The PVA, SL and alcohol were selected as the binder, dispersant and solvent throughout the study, respectively. After milled for 1 h to disintegrate the agglomerated particles, the slurry was fed into the preheated closed-circulation drying chamber (BGP-25) by a peristaltic pump. The inlet temperature and the outlet temperature were 180 ℃ and 130 ℃, respectively. During the granulated process, nitrogen was used as the shielding gas. Thereafter, the granulated powders were transferred into a

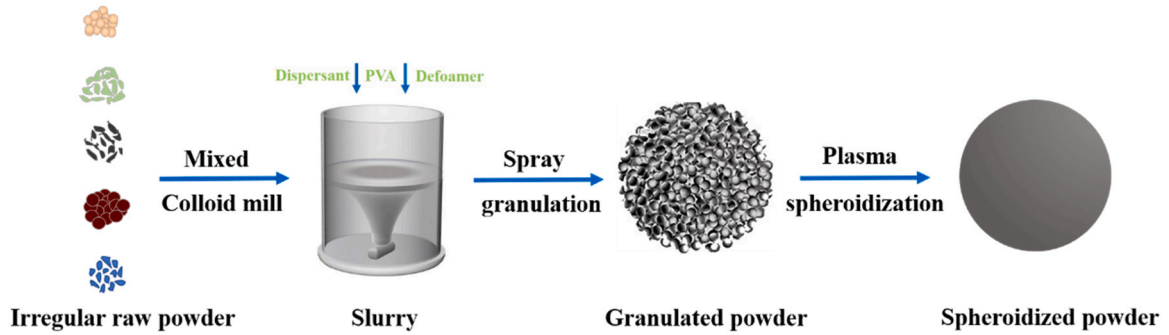

Fig. 2. Schematic diagram of the experimental procedure. This process includes: preparation of slurry, spray granulation, and plasma spheroidization.

Table 1
Parameters of the utilized plasma spheroidization.

Process parameter	Values
Primary gas (Ar)	45 slpm
Centre gas (Ar)	20.5 slpm
Secondary gas (H_2)	3.5 slpm
Powder feeding rate	26–30 g/min
Plasma power	40 KW

plasma spheroidizing system (Tekna Nano-15) with the mixed gas by water cooled probe to prepare the target powders. At the molten stage, alloying took place and spherical droplets were formed because of the surface tension. When the droplets passed away the plasma torch, they rapidly cooled and solidified to form spherical particles. Detailed parameters of plasma spheroidization process are listed in Table 1.

2.2. Characterization

Phase compositions of spray granulation and plasma spheroidization powders were identified via an X-ray diffraction (XRD, Bruker D8) with Cu Kα radiation (λ = 1.54 Å). The experiments were conducted using a scan rate of 4°/min and the diffraction angle (2θ) varied from 20° to 90°. Crystal structure parameters were calibrated by the software of Jade 6.0. The powders obtained after every stage during process for microstructural observation were firstly mounted using resin, and mechanical-polished until the surface was as smooth as a mirror. Scanning electron microscope (SEM, FEI Quanta 200 F) equipped with energy dispersive spectrometer (EDS, Xplore 30) and electron probe microanalysis (EPMA, Shimadzu 8050 G) were applied to observe the morphology and element distribution. Particle size and its distribution were measured using light scattering by a laser particle analyzer (Malvern, Mastersizer 3000). The results were generally recorded by D_α, including D_{10}, D_{50}, D_{90} and D_{av}. Flowability and apparent density of the powders were determined analyzed by a Hall-flow meter. The oxygen, hydrogen, carbon and nitrogen concentrations were tested by using an O/N/H analyzer (Leco, ON 736) and a C/S analyzer (Leco, CS 884), respectively. Nanoindentation (hardness) tests of the powder was carried out by a nanoindentation tester (NYSE: A, G200) and the Young's modulus was achieved from the nano-indentation measurement. The spheroidization ratio of the spheroidized powder was analyzed by the formula as following [23]:

$$\mu = \frac{N_A}{N_B}$$

where μ, N_A, and N_B represent the spheroidization ratio, the number of spherical powder particles, and the total number of powder particles, respectively. To improve reliability, three SEM images which contain at least two hundred powder particles were chosen, and the average value was taken.

3. Results and discussion

3.1. Powder morphology and structure of SG and PS

SEM images showing the surface morphology of granulated MoNbTaWZr powder and the detailed formation of particles with different shapes are shown in Fig. 3. It can be seen from Fig. 3(a) that the granulated particles were agglomerates of raw powders

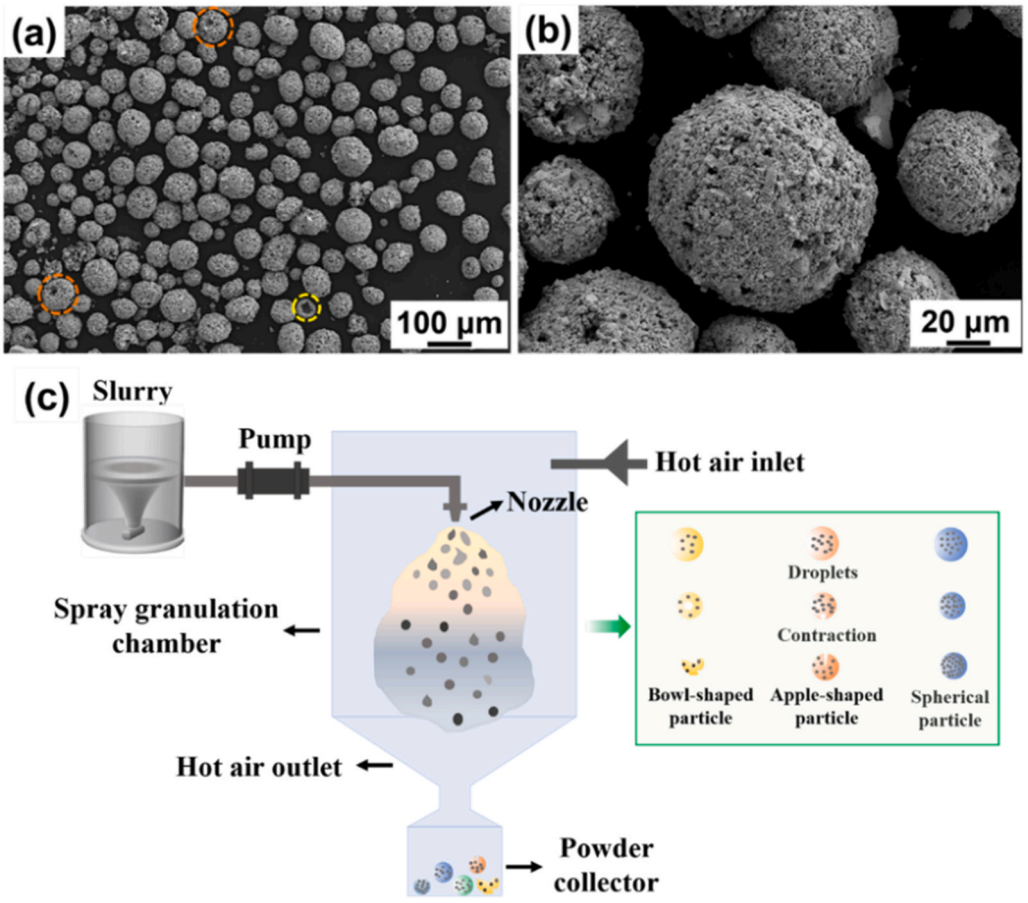

Fig. 3. (a) SEM image of granulated MoNbTaWZr powder (b) SEM image of a single granulated MoNbTaWZr powder (c) schematic of spray granulation and formation sketch of bowl-shaped particle, apple-shaped particle and spherical particle.

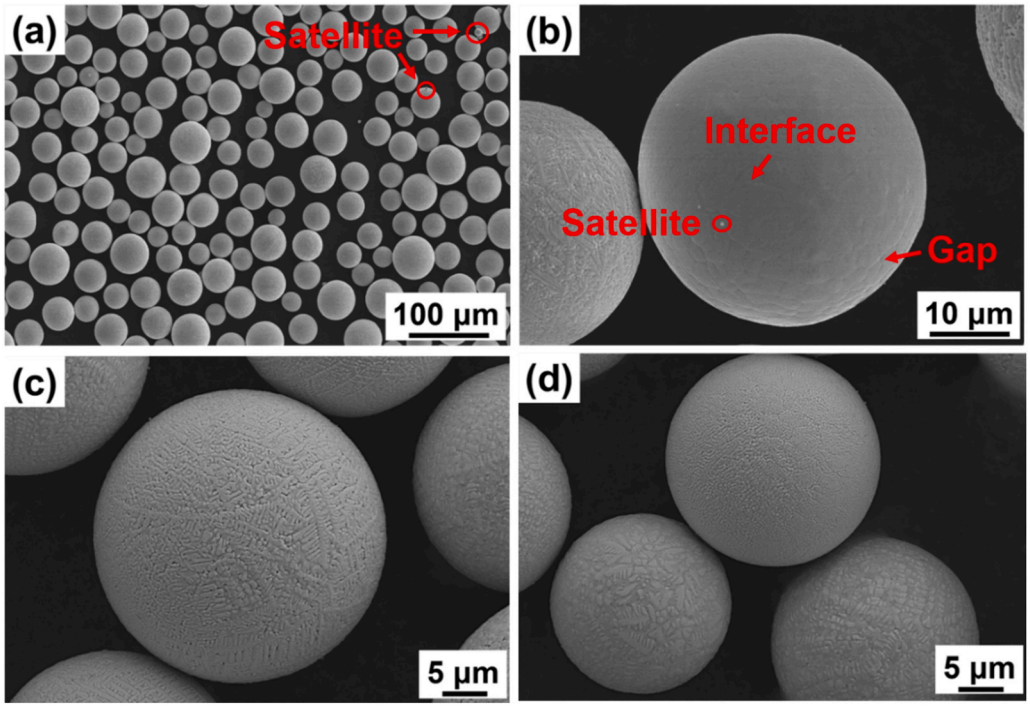

Fig. 4. (a) SEM image of granulated MoNbTaWZr powder after plasma spheroidization (b), (c) and (d) typical morphology of spheroidized MoNbTaWZr powder.

particles. Most of the powder particles were spherical, although bowl-shaped particle and apple-shaped particles marked by yellow and orange circles respectively were also observed. This is mainly related with the solidification process that the droplet underwent during SG, which plays a major role in deciding the powder characteristics. Morphology evolution process of different shape particles are summarized in Fig. 3(c). When a continuous stirred slurry was pumped to the spray granulation device, a large number of small droplets of liquid binder formed. Actually, a single droplet contained solid would experience two drying stages during granulation [24]. At the initial period, contraction of particle and decrease of diameter occurred due to the water evaporation directly from the surface. If the water had sufficient time to evaporate and the particle concentration was homogenous in the radial direction of the droplet, thus spherical granulated particles formed due to the surface tension [25]. Thereafter, wet porous agglomerate structures formed and the diameter did not change any more as the water evaporated through the pores. Otherwise, the water migrated to the surface, resulting in the formation of vacancies in the droplet. In this case, voids formed and subsequently under the action of gas vapor pressure within the porous shell, droplet would break into fragments [26]. Finally, droplet became hollow granule. Moreover, the granulated powder exhibited fine porosity generated by evaporation of water and PVA [22] according to the high magnification surface image in Fig. 3(b). It also can be observed that the surface was rough, which was affected by the diameter discrepancy of raw powder particles. Narrow and uniform particle size would be easier to granulate smoother surface. And it's worth to try and study in the future.

Fig. 4 depicts the SEM morphology of the spheroidized MoNbTaWZr powder. Low magnification surface image (Fig. 4(a)) shows that the powders after PS were well spherical in shape with a smooth and burr-free surface compared with the granulated powder. Good sphericity is benefit to enhance the flowability and compactibility. As observed, satellites where two spheres joined were noticeable. The occurrence of satellite attached on the particle surface were induced by particle flying during PS. It was evidenced that particles in different diameters behaved distinguishing heat absorption and trajectory motion inside the plasma [27]. Small particles with higher velocity, which would firstly solidified, collided with large droplets that were not completely solidified yet. As a result, adhesion, partial penetration or fusion between particles occurred, causing finer particles sticking on the surface of large particles [28]. Besides, it is visible that for each particle, the microstructure of the particles appeared to vary. Typical surface morphologies are displayed in Fig. 4(b) ~ (d). Interfaces and gaps were clearly observed on the surface in Fig. 4(b), while dendritic structure and equiaxed-type structure with small pinholes were shown in Fig. 4(c) and (d). The development of the typical microstructure was strongly related with the effect of solidification shrinkage. Rapid cooling rate and inhibition of grain growth promoted the dendritic structure and equiaxed-type structure to form [29,30].

In order to confirm the elements distribution on the powder surface after PS, EDS technique was conducted (Fig. 5). Before PS, it was just sticking the Mo, Nb, Ta, W, and ZrH_2 slurry together via SG. However, if these granules could not melt completely during PS, the separation of any element would cause a composition change. The point EDS chemical composition collected from the powder was listed in upper left corner, suggesting a nearly equimolar ratio of each element. In addition, element mapping revealed a homogeneous distribution of Mo, Nb, Ta, W and Zr within the resolution limit of the technology.

SEM image and EDS spectrometer of cross-section of the spheroidized MoNbTaWZr powder are exemplified in Fig. 6. According to the observation, the powders were of complete spherical appearance and a dense internal structure without visible micro-crack and pores were found from Fig. 6(a). A higher magnification image of the selected square region is shown in Fig. 6(b). It is noticed that the internal structure of the powder consisted of major dendrites in light gray, indicating micro-segregation in the powder. The corresponding EDS elemental maps and atomic ratio in Fig. 6(c) suggested an identical results. The distribution of elements in the interior listed in the table was uniform and near-equimolar ratio of each element, which was in good agreement with the results in Fig. 5. In order to

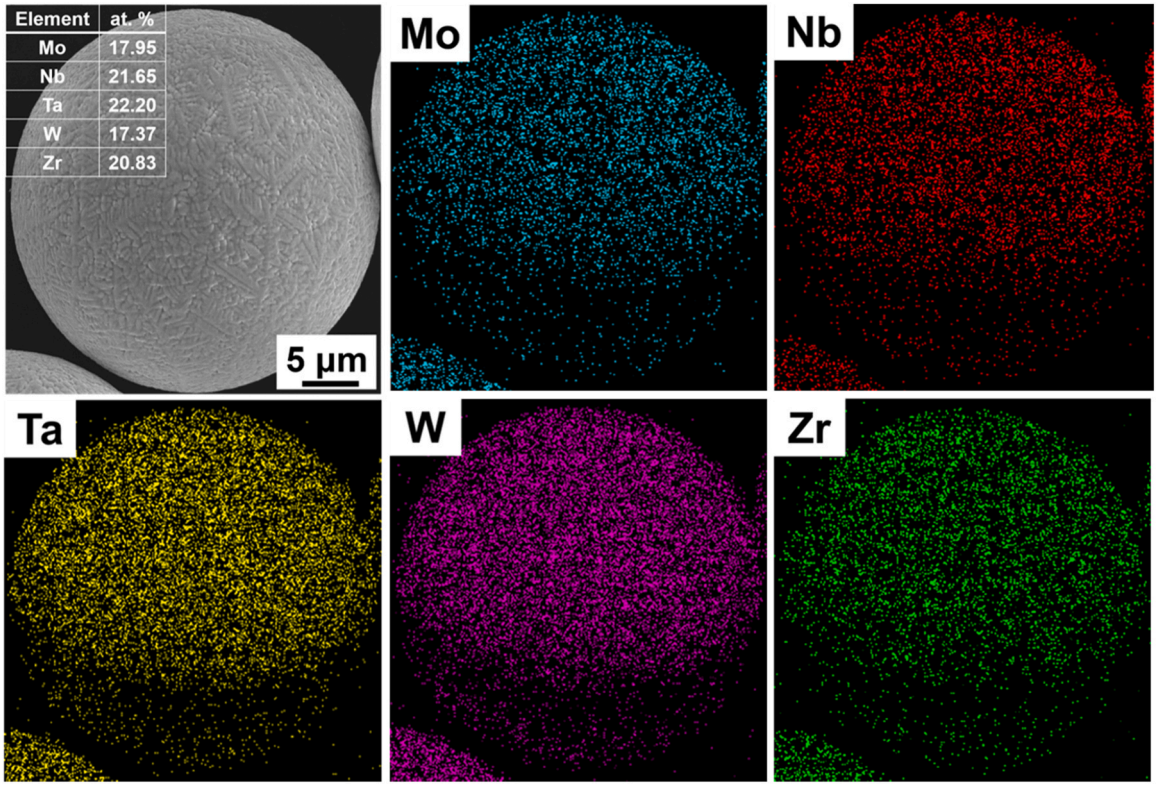

Fig. 5. Point EDS analysis and elemental distribution of MoNbTaWZr powder after plasma spheroidization.

investigate the micro-segregation furtherly, point EDS was conducted in dendrite (A) and inter-dendrite (B), and the data are listed in Fig. 6(d). Elements, higher melting point, Ta, W, enriched at the dendrite, while element, lower melting point, Zr was located at the inter-dendrite. It has been proved that the micro-segregation was caused by Zr [13]. On the one hand, the micro-segregation in the powder would be promoted by a positive mixing enthalpy as Zr has a positive mixing enthalpy with Ta [31]. On the other hand, it is prone

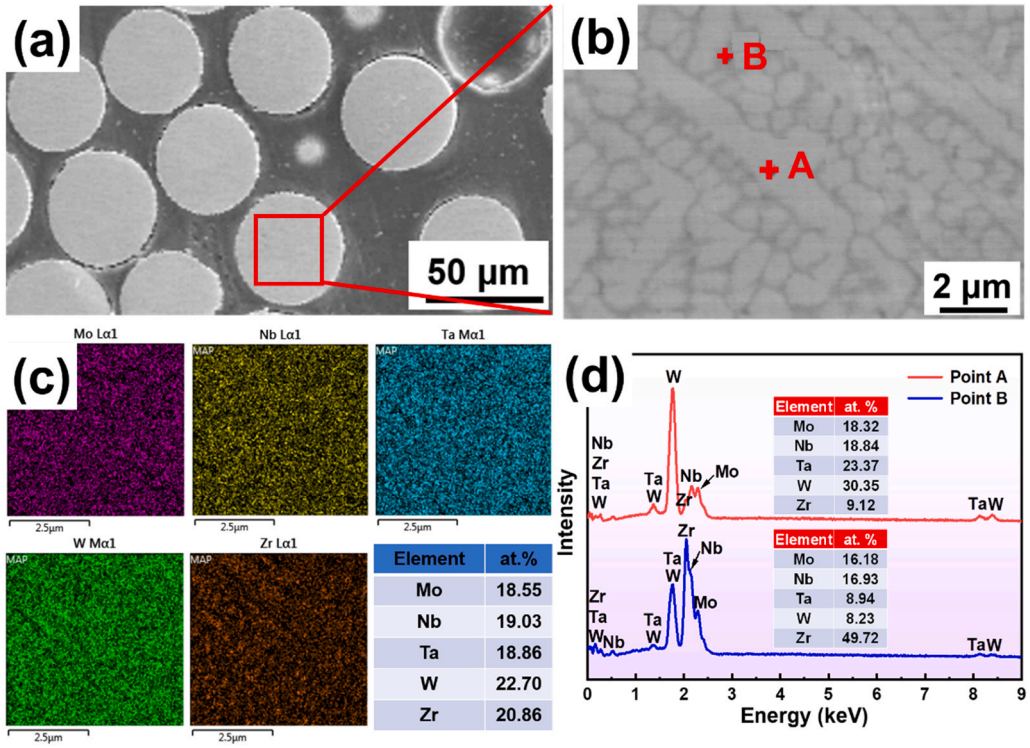

Fig. 6. SEM morphology and EDS spectrometer of the spherical powder: (a) cross-section SEM image (b) high-magnification SEM image of (a) marked by red square (c) elemental mapping of cross-section (d) EDS spectrum and elemental atomic ratio of point A and B in (b).

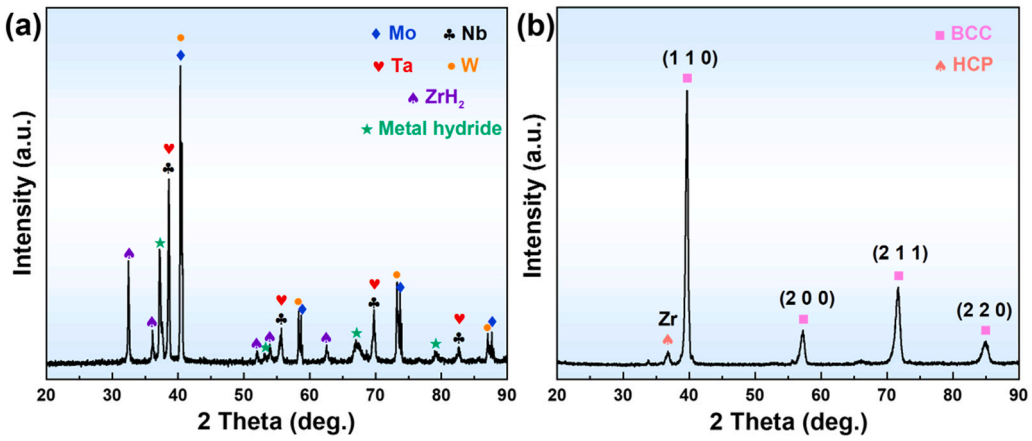

Fig. 7. XRD spectrum of the spherical powder: (a) spray granulated powder (b) plasma spheroidized powder.

to form micro-segregation due to severe local lattice distortions and charge transfer effect, which was attributed to the larger atomic radius of Zr than Mo, Nb, Ta and W [15]. The same phenomenon of Zr-rich in the MoNbTaWZr alloy powder was also found in our previous study [32].

XRD analysis was also conducted to understand the detailed phase component transformation from SG to PS. The corresponding XRD patterns are shown in Fig. 7. It can be seen that the powder prepared after SG was composed of five raw materials and small amount of metal hydrides. The existence of metal hydrides was related with the raw powder, ZrH_2. It would decompose into Zr and H_2 when the powder ZrH_2 absorbed heat during SG. Then the other metals reacted with H_2, which led to the formation of metal hydrides. Therefore, the relative peaks were observed in the XRD patterns. No oxide phase was in observation, which might be associated with low contents that could not be detected by conventional XRD. However, the diffraction peaks were varied after PS. From Fig. 7(b), typical peaks of BCC structures and a small peak of HCP (Zr), which were corresponding to light gray and dark gray respectively shown in Fig. 6(b) were observed after PS. Metal hydride phase was absent in the spheroidized powder, due to the ultra-high temperature of plasma torch. In addition, the peaks in Fig. 7(b) were clearly broad. It was believed responsible for an increase of sub-grain boundaries due to the rapid cooling rate [33].

3.2. Purity

EPMA was carried out to further investigate oxygen distribution in the granulated and spheroidized powder, as shown in Fig. 8. The transition of color from blue to orange represents a progressive

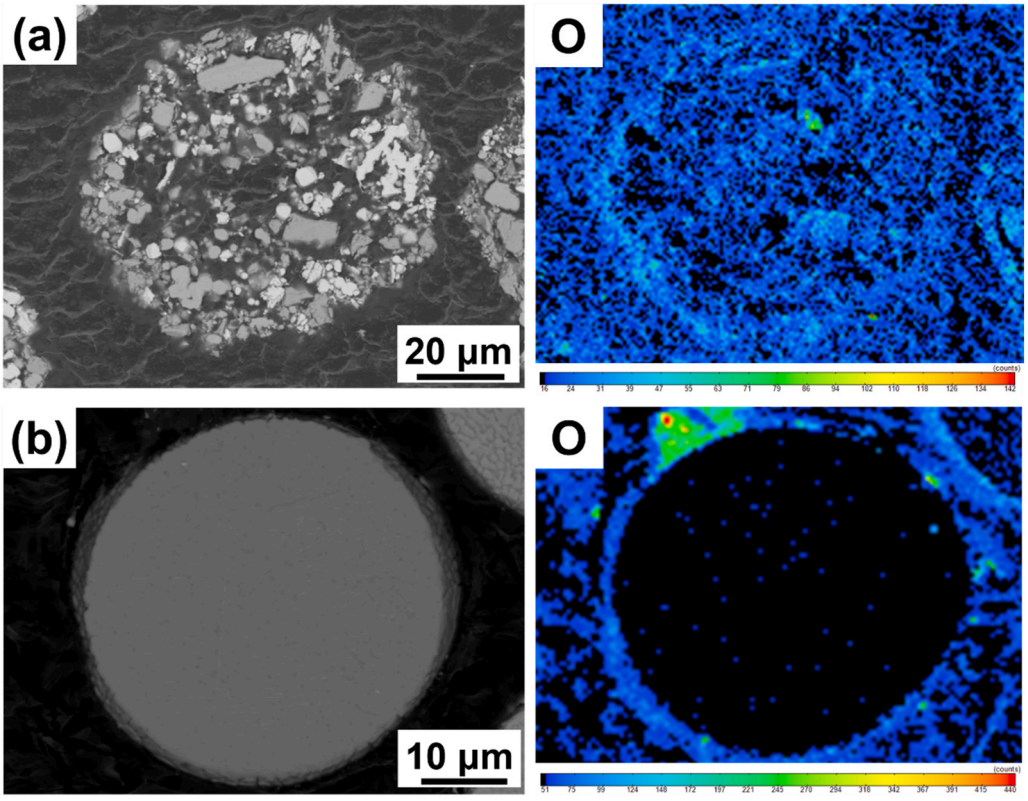

Fig. 8. Cross-section of a single granulated powder and spheroidized powder (a) BSE-SEM image (b) EPMA mapping result of O element (c) BSE-SEM image (d) EPMA mapping result of O element.

Table 2
O/H/C/N content of granulated and spheroidized MoNbTaWZr powder.

Process method	O /ppm	H/ppm	C/ppm	N/ppm
Spray granulation	6050	5035	2684	144
Plasma spheroidization	750	122.9	254.9	15.7

increase in the percentage. Oxidation was observed to be covered both on the cross-sectioned surface of the granulated and spheroidized powder, whereas the oxygen content of the granulated powder was relatively higher than that of spheroidized powder. The specific content of oxygen, hydrogen, carbon, and nitrogen was measured and the results were listed in Table 2. The PS treatment significantly reduced the hydrogen content from 6050 ppm to 750 ppm. The content of oxygen, carbon, and nitrogen were also decreased as approximately an order of magnitude. High purity atmosphere and high operating temperature were the possible reasons. Firstly, high purity atmosphere during PS process avoided the generation of oxidation contamination from ambient effectively. Secondly, the usage of hydrogen as the secondary gas in PS treatment, and the residual nitrogen as the protective gas in SG process would fetch high enthalpy of plasma torch and high thermal conductivity to particles [27]. Therefore, residual oxygen and the produced oxides would evaporate from the powder surface due to the ultra-high temperature. On the other hand, evaporation of small particles would decrease the specific surface area, leading a reduction of oxygen [34]. Another issue should be noted is that hydrogen or carbon are usually regarded as a deoxidation agent [35]. The oxides would react with them to form water or carbide gas. Thereafter, the water could evaporate because of the high temperature during PS treatment. It can be concluded that the impurities were eliminated through EPMA and XRD analysis, ensuring the purity of MoNbTaWZr target powder.

Detailed thermodynamic analysis calculated by HSC 6.0 Chemistry software was conducted to help understand the reduction mechanism. Fig. 9(a) depicts the calculation results of oxygen potential. As seen, all of the reactions had negative Gibbs free energy between room temperature to 3000 K. That is to say, oxidation could happen spontaneously during SG process while nitrogen was used as a sheath gas. Generally speaking, the more negative the Gibbs free energy of a equation in the same process condition, the more priority the oxidation happens, and the more stable the oxides produce [36]. Based on the thermodynamic calculation analysis displayed in Fig. 9(a), a series of oxides, for instance, ZrO_2, NbO, Ta_2O_5, NbO_2, Nb_2O_5, WO_2, WO_3, MoO_2 and MoO_3 would form, and the most stable was ZrO_2. The Gibbs free energy for hydrogen and carbon oxygen reactions are shown in Fig. 9(b), (c) and (d). It could be found that the hydrogen-reduced ZrO_2 and carbon-reduced ZrO_2 would form metals, H_2O, CO_2, and CO at 6573.15 K and 2473.15 K, respectively. Subsequently, the resultants which attached on the surface would be eliminated at high temperature, causing a decrease in the oxygen content. However, it was difficult to remove the impurities completely as a small quantity of impurities were produced inside the powder during SG.

3.3. Particle size distribution

The particle size distribution (PSD) of MoNbTaWZr powders after SG and PS are presented in Fig. 10. The average particle size of granulated powders was 45.7 μm, while after PS a slight shift to the left with a D_{av} = 43.2 μm was found. These revealed a decrease of the powder particle size. It was attributed to the shrinkage of the

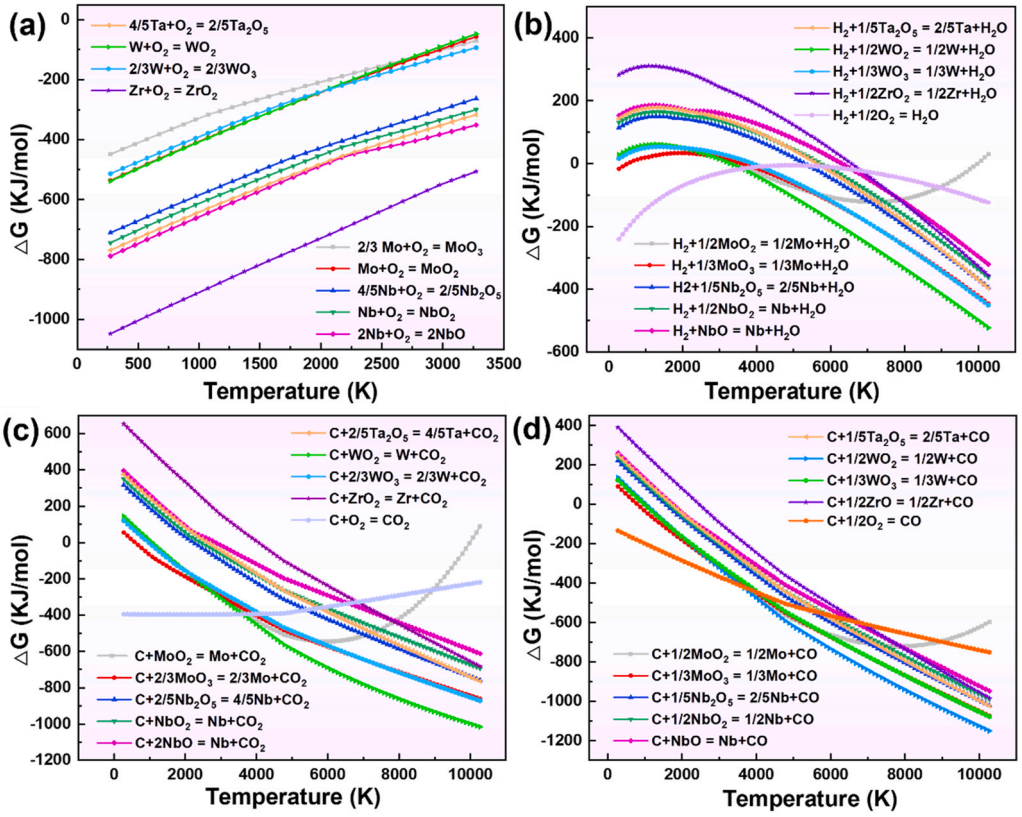

Fig. 9. Thermodynamic calculations: (a) calculation results of oxygen potential (b) Gibbs free energy via temperature curves between oxides and H_2 (c), (d) Gibbs free energy via temperature curves between oxides and carbon.

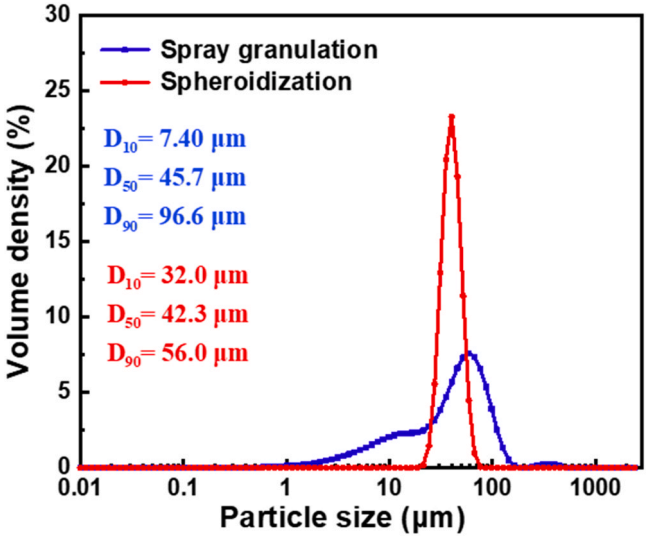

Fig. 10. Particle size distribution curves of granulated powders and spheroidized powders.

granulated powders and dense internal structure after PS, which was verified in cross-section depicted in Fig. 8(b). The spheroidized PSD became narrower with a range from 21 μm to 76 μm, whereas the granulated PSD was broad with D_{10} (fine particle) of 7.40 μm, D_{90} (coarse particle) of 96.6 μm, respectively. Another issue was the number of finer particles decreased. As we all know, the temperature of plasma torch is more than 10^4 K. The granulated particles would melt immediately when they were fed into plasma flow. Smaller powders, especially the surface portion, absorbed sufficient heat and completely vaporized. Excessive evaporation of finer powder particles was the dominant reason of the reduction of finer particles [37]. In addition, smaller agglomerates adhered together or melted into a large droplet due to collision, and eventually solidified in formation of a whole particle [34]. Therefore, particles (< 20 μm) would decrease significantly after PS, making the apparent density increased.

3.4. Property

After characterizing the PSD, phase component, purity and morphology, the property of granulated and spheroidized powder was then measured through spheroidization ratio, flowability, repose angle and apparent density. It can be observed that the powder with high spheroidization ratio (98.4 %) was obtained after PS, as shown in Table 3. A higher spheroidization ratio benefited a good flowability and high apparent density. Therefore, the flowability of the powders was significantly improved from 28.93 s•(50 g)$^{-1}$ to 8.89 s•(50 g)$^{-1}$. Fig. 11 displays the corresponding repose angle of granulated and spheroidized powders after Hall flow test. Both of the stacking morphologies showed a relative smooth slope. However, the repose angle of spherical powder decreased from 32 ± 0.5° to 22 ± 0.5°, which was a good confirmation of spheroidization. The apparent density of spheroidized powder reached 7.27 g•cm^{-3}, which was much higher than that of granulated powders. It is known that powder shape, PSD, and surface morphology play a prominent role in the flowability and apparent density. Good shape of sphericity, smooth surface, compact structures and high spheroidization ratio after PS treatment reduced the contact area, mechanical interlock and friction coefficient between particles. The decrease of finer particles and a narrow PSD further increased the flowability and apparent density [21,33]. Powders with good flowability and high apparent density are required for PM, AM, and thermal spraying.

The nano-hardness and Young's modulus came from nano-indentation were examined by a nano-indenter on the cross-section of spherical MoNbTaWZr RHEA powder. The obtained nano-hardness and Young's modulus were 6.46 GPa and 86.45 GPa, respectively. Solid solution strengthening caused by lattice distortion and nano-scale dendritic structure due to rapid cooling rate were therefore believed to responsible for the ultra-high nano-hardness of the powder. Looking into the atomic radius, the atomic radius of Zr was larger than that of other four metal elements', which was significantly result in lattice distortion [38]. The ultra-fast cooling rate induced by PS reduced the max diffusion distance, resulting in a much narrow dendritic structure, shown in Fig. 6(b). Thus, the refinement of dendritic structures enhanced the hardness.

Table 3
Spheroidization ratio, flowability, apparent density of granulated and spheroidized MoNbTaWZr powder.

Process method	Spheroidization ratio / %	Flowability /s• (50 g)$^{-1}$	Apparent density / g•cm^{-3}
Spray granulation	70.5	28.93	2.47
Plasma spheroidization	98.4	8.89	7.27

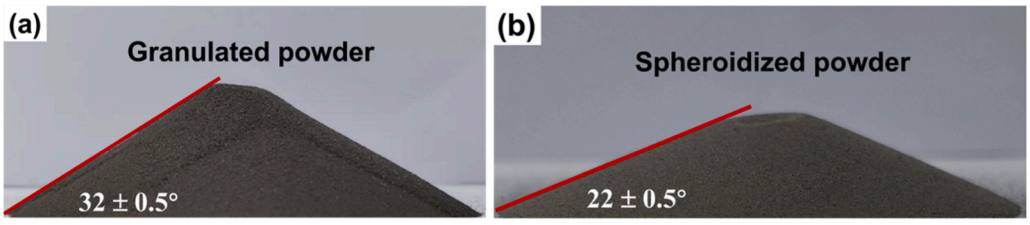

Fig. 11. Repose of the MoNbTaWZr powder: (a) granulated powders (b) spheroidized powders.

4. Conclusions

A comprehensive study of fabrication method on spherical MoNbTaWZr RHEA powder was investigated in this paper. Through comparative researches on microstructure, morphology, PSD, purity, and property, a feasible technique combined with SG and PS was proposed to prepare spherical MoNbTaWZr RHEA powder. The main conclusions were drawn as follows.

(1) After PS treatment, spherical MoNbTaWZr powder had a prominent BCC solid solution and a small amount of HCP (Zr) phase.
(2) Compared with granulated powder, the spheroidized powder was denser with a good sphericity. The spheroidization percentage was 98.4 %.
(3) The D_{10}, D_{50}, D_{90} and D_{av} of spheroidized powders were 32.0 μm, 42.3 μm, 56.0 μm and 43.2 μm, whereas the granulated powders were broad with D_{10} of 7.40 μm, D_{90} of 96.6 μm, and D_{av} of 51.4 μm, respectively.
(4) The obtained spherical powder had high purity, for that the content of oxygen, hydrogen, carbon, and nitrogen were all at ppm.
(5) The spherical powder had excellent flowability (8.89 s/50 g), apparent density (7.27 g/cm^3), and high nano-hardness (6.46 GPa).

CRediT authorship contribution statement

Ming Xia: Conceptualization, Methodology, Investigation, Data curation, Visualization, Writing – original draft, Writing – review & editing. **Yongxiong Chen:** Investigation. **Zhenggang Luo:** Methodology. **Xiubing Liang:** Supervision, Funding acquisition, Resources, Project administration. **Baolong Shen:** Resources, Project administration, Supervision.

Data Availability

The data that has been used is confidential.

Declaration of Competing Interest

The authors declare that they have no known competing financial interests or personal relationships that could have appeared to influence the work reported in this paper.

Acknowledgements

The authors would like to acknowledge the financial support from the National Key Research and Development Program of China (Grant N. 2018YFC1902400), the National Natural Science Foundation of China (Grant N. 51975582), Jiangsu Provincial Key Research and Development Program (No. BE2021088).

References

[1] J.W. Yeh, S.J. Lin, J.Y. Gan, T.S. Chin, T.S. Shun, C.H. Tsau, S.Y. Chang, Nanostructured high-entropy alloys with multiple principal elements: novel alloy design concepts and outcomes, Adv. Eng. Mater. 6 (2004) 299–303.
[2] B. Cantor, I.T.H. Chang, P. Knight, A.J.B. Vincent, Microstructural development in equiatomic multicomponent alloys, Mat. Sci. Eng. A-Struct. 375 375-377 (2004) 213–218.
[3] J.-T. Liang, K.-C. Cheng, S.-H. Chen, Effect of heat treatment on the phase evolution and mechanical properties of atomized AlCoCrFeNi, High. -entropy Alloy. Powders, J. Alloy. Compd. 803 (2019) 484–490.
[4] J. Lehtonen, Y. Ge, N. Ciftci, O. Heczko, V. Uhlenwinkel, S.-P. Hannula, Phase structures of gas atomized equiatomic CrFeNiMn high entropy alloy powder, J. Alloy. Compd. 827 (2020) 154142.
[5] Z.B. An, S.C. Mao, Y.N. Liu, L. Wang, H. Zhou, B. Gan, Z. Zhang, X.D. Han, A novel HfNbTaTiV high-entropy alloy of superior mechanical properties designed on the principle of maximum lattice distortion, J. Mater. Sci. Technol. 79 (2021) 109–117.
[6] C. Lee, Y. Chou, G. Kim, M.C. Gao, K. An, J. Brechtl, C. Zhang, W. Chen, J.D. Poplawsky, G. Song, Y. Ren, Y.-C. Chou, P.K. Liaw, Lattice-distortion-enhanced yield strength in a refractory high-entropy alloy, Adv. Mater. 32 (2020) 2004029.
[7] Z.F. Lei, X.J. Liu, Y. Wu, H. Wang, S.H. Jiang, S.D. Wang, X.D. Hui, Y.D. Wu, B. Gault, P. Kontis, D. Raabe, L. Gu, Q.H. Zhang, H.W. Chen, H.T. Wang, J.B. Liu, K. An, Q.S. Zeng, T.-G. Nieh, Z.P. Lu, Enhanced strength and ductility in a high-entropy alloy via ordered oxygen complexes, Nature 563 (2018) 546–550.
[8] N.B. Hua, W.J. Wang, Q.T. Wang, Y.X. Ye, S.H. Lin, L. Zhang, Q.H. Guo, J. Brechtl, P.K. Liaw, Mechanical, corrosion, and wear properties of biomedical Ti–Zr–Nb–Ta–Mo high entropy alloys, J. Alloy. Compd. 861 (2021) 157997.
[9] G.S. Jawaharram, C.M. Barr, A.M. Monterrosa, K. Hattar, R.S. Averback, S.J. Dillon, Irradiation induced creep in nanocrystalline high entropy alloys, Acta Mater. 182 (2020) 68–76.
[10] W.M. Guo, B. Liu, Y. Liu, T.C. Li, A. Fu, Q.H. Fang, Y. Nie, Microstructures and mechanical properties of ductile NbTaTiV refractory high entropy alloy prepared by powder metallurgy, J. Alloy. Compd. 776 (2019) 428–436.
[11] O.N. Senkov, G.B. Wilks, J.M. Scott, D.B. Miracle, Mechanical properties of $Nb_{25}Mo_{25}Ta_{25}W_{25}$ and $V_{20}Nb_{20}Mo_{20}Ta_{20}W_{20}$ refractory high entropy alloys, Intermetallics 19 (2011) 698–706.
[12] T. Xiong, S.J. Zheng, J.Y. Pang, X.L. Ma, High-strength and high-ductility $AlCoCrFeNi_{2.1}$ eutectic high-entropy alloy achieved via precipitation strengthening in a heterogeneous structure, Scr. Mater. 186 (2020) 336–340.
[13] T.X. Li, W.N. Jiao, J.W. Miao, Y.P. Lu, E.Y. Guo, T.M. Wang, T.J. Li, P.K. Liaw, A novel ZrNbMoTaW refractory high-entropy alloy with in-situ forming heterogeneous structure, Mater. Sci. Eng. A 827 (2021) 142061.
[14] S.G. Yang, J. Lu, F.Z. Xing, L.J. Zhang, Y. Zhong, Revisit the VEC rule in high entropy alloys (HEAs) with high-throughput CALPHAD approach and its applications for material design-A case study with Al–Co–Cr–Fe–Ni system, Acta Mater. 192 (2020) 11–19.
[15] Y. Tong, S.J. Zhao, H.B. Bei, T. Egami, Y.W. Zhang, F.X. Zhang, Severe local lattice distortion in Zr- and/or Hf-containing refractory multi-principal element alloys, Acta Mater. 183 (2020) 172–181.
[16] Y.G. Tong, L.H. Bai, X.B. Liang, Y.X. Chen, Z.B. Zhang, J. Liu, Y.J. Li, Y.L. Hu, Influence of alloying elements on mechanical and electronic properties of NbMoTaWX (X = Cr, Zr, V, Hf and Re) refractory high entropy alloys, Intermetallics 126 (2020) 106928.
[17] M. Moorehead, K. Bertsch, M. Niezgoda, C. Parkin, M. Elbakhshwan, K. Sridharan, C. Zhang, D. Thoma, A. Couet, High-throughput synthesis of Mo-Nb-Ta-W high-entropy alloys via additive manufacturing, Mater. Des. 187 (2020) 108358.
[18] N.F. Shkodich, K.V. Kuskov, A.S. Sedegov, I.D. Kovalev, A.V. Panteleeva, Y.S. Vergunova, Y.B. Scheck, E. Panina, N. Stepanov, I. Serhiienko, D. Moskovskikh, Refractory TaTiNb, TaTiNbZr, and TaTiNbZrX (X = Mo, W) high entropy alloys by combined use of high energy ball milling and spark plasma sintering: Structural characterization, mechanical properties, electrical resistivity, and thermal conductivity, J. Alloy. Compd. 893 (2022) 162030.
[19] B.H. Duan, Y.R. Yu, X.L. Liu, D.Z. Wang, Z.Z. Wu, A novel non-equiatomic $(W_{35}Ta_{35}Mo_{15}Nb_{15})_{95}Ni_5$ refractory high entropy alloy with high density fabricated by powder metallurgical process, Metals 10 (2020) 1436.
[20] T. Fedina, J. Sundqvist, J. Powell, A.F.H. Kaplan, A comparative study of water and gas atomized low alloy steel powders for additive manufacturing, Addit. Manuf. 36 (2020) 101675.
[21] B. Liu, H. Duan, L.S. Li, C.S. Zhou, J.Y. He, H.B. Wu, Microstructure and mechanical properties of ultra-hard spherical refractory high-entropy alloy powders fabricated by plasma spheroidization, Powder Technol. 382 (2021) 550–555.
[22] Z.H. Hao, Y.H. Chen, Q.L. Zhang, P. Wang, Y.C. Shu, J.L. He, Fabrication of spherical Ti-6Al-4V powder by RF plasma spheroidization combined with mechanical alloying and spray granulation, Adv. Powder Technol. 33 (2022) 103379.
[23] Z.H. Hao, Y.H. Chen, Z.H. Fu, S. Guo, X.Y. Zhu, F. Zhou, Y.C. Shu, J.L. He, A comparative study on spheroidization of sodium reduced and hydrogenation-dehydrogenation tantalum powder by RF plasma, Int. J. Refract. Met. Hard Mater. 100 (2021) 105624.
[24] Y.D. Pour, B. Krasovitov, A. Fominykh, Z. Hashemloo, A. Kharaghani, E. Tsotsas, A. Levy, Intensification of spray drying granulation process by gas absorption accompanied by chemical dissociation reactions, Chem. Eng. J. 433 (2022) 133566.
[25] L. Liu, Z.S. Li, N.S. Cai, Oxidization and reduction kinetics of a manganese oxygen carrier granulated with the spray drying method at a tonnage scale for chemical looping combustion, Fuel 303 (2021) 121267.
[26] J. Chen, H. Yang, C.-M. Xu, J.-G. Cheng, Y.-W. Lu, Preparation of ZrO_2 microspheres by spray granulation, Powder Technol. 385 (2021) 234–241.
[27] K.S. Sista, A.P. Moon, G.R. Sinha, B.M. Pirjade, S. Dwarapudi, Spherical metal powders through RF plasma spherodization, Powder Technol. 400 (2022) 117225.
[28] D. Beckers, N. Ellendt, U. Fritsching, V. Uhlenwinkel, Impact of process flow conditions on particle morphology in metal powder production via gas atomization, Adv. Powder Technol. 31 (2020) 300–311.
[29] A.T. Ernst, P. Kerns, A. Nardi, H.D. Brody, A.M. Dongare, S.-W. Lee, V.K. Champagne, S.L. Suib, M. Aindow, Surface states of gas-atomized Al 6061 powders – Effects of heat treatment, Appl. Surf. Sci. 534 (2020) 147643.

[30] M. Akkaş, M. Boz, Investigation of the compressibility and sinterabilty of AZ91 powder production and particle production by gas atomisation method, J. Magnes. Alloy 7 (2019) 400–413.
[31] M. Akmal, H.-K. Park, H.J. Ryu, Plasma spheroidized MoNbTaTiZr high entropy alloy showing improved plasticity, Mater. Chem. Phys. 273 (2021) 125060.
[32] M. Xia, Y.X. Chen, K.W. Chen, Y.G. Tong, X.B. Liang, B.L. Shen, Synthesis of WTaMoNbZr refractory high-entropy alloy powder by plasma spheroidization process for additive manufacturing, J. Alloy. Compd. 917 (2022) 16550.
[33] Q.Q. Li, B.C. Zhang, Y.J. Wen, G. Chen, Y.H. Wang, P. Wang, X.H. Qu, A comprehensive study of tantalum powder preparation for additive manufacturing, Appl. Surf. Sci. 593 (2022) 153357.
[34] B.W. Liu, G.M. He, Y. Liu, M.F. Yue, L.X. Lian, High-quality spherical zirconium alloy powders prepared by thermal plasma treatment for additive manufacturing, Mater. Lett. 288 (2021) 129360.
[35] Z.W. Dong, Y. Xia, X.Y. Guo, J.L. Zhao, L.F. Jiang, Q.H. Tian, Y. Liu, Direct reduction of upgraded titania slag by magnesium for making low-oxygen containing titanium alloy hydride powder, Powder Technol. 368 (2020) 160–169.
[36] S.-L. Li, P. Hu, Y.-G. Zuo, H.-R. Xing, J.-Y. Han, S.-W. Ge, X.-J. Hua, B.-L. Hu, C.-J. Cui, K.-S. Wang, Precise control of oxygen for titanium-zirconium-molybdenum alloy, Int. J. Refract. Met. Hard Mater. 103 (2022) 105768.
[37] Z.Q. Yan, M. Xiao, X.H. Mao, K. Khanlari, Q. Shi, X. Liu, Fabrication of spherical WC-Co powders by radio frequency inductively coupled plasma and a consequent heat treatment, Powder Technol. 385 (2021) 160–169.
[38] S.H. Chen, J.S. Zhang, S. Guan, T. Li, J.Q. Liu, F.F. Wu, Y.C. Wu, Microstructure and mechanical properties of WNbMoTaZrx (x = 0.1, 0.3, 0.5, 1.0) refractory high entropy alloys, Mater. Sci. Eng. A 835 (2022) 142701.